Leveraging hierarchical self-assembly pathways for realizing colloidal photonic crystals

Rao, Abhishek B; Shaw, James; Neophytou, Andreas; Morphew, Daniel; Sciortino, Francesco; Johnston, Roy L; Chakrabarti, Dwaipayan

DOI:
10.1021/acsnano.9b07849

ACS NANO

www.acsnano.org

ARTICLE

Leveraging Hierarchical Self-Assembly Pathways for Realizing Colloidal Photonic Crystals

Abhishek B. Rao,[§] James Shaw,[§] Andreas Neophytou,[§] Daniel Morphew, Francesco Sciortino, Roy L. Johnston, and Dwaipayan Chakrabarti*

Cite This: *ACS Nano* 2020, 14, 5348−5359

Read Online

ACCESS | Metrics & More | Article Recommendations | Supporting Information

ABSTRACT: **Colloidal open crystals are attractive materials, especially for their photonic applications. Self-assembly appeals as a bottom-up route for structure fabrication, but self-assembly of colloidal open crystals has proven to be elusive for their mechanical instability due to being low-coordinated. For such a bottom-up route to yield a desired colloidal open crystal, the target structure is required to be thermodynamically favored for designer building blocks and also kinetically accessible *via* self-assembly pathways in preference to metastable structures. Additionally, the selection of a particular polymorph poses a challenge for certain much sought-after colloidal open crystals for their applications as photonic crystals. Here, we devise hierarchical self-assembly pathways, which, starting from designer triblock patchy particles, yield in a cascade of well-separated associations first tetrahedral clusters and then tetrastack crystals. The designed pathways avoid trapping into an amorphous phase. Our analysis reveals how such a two-stage self-assembly pathway *via* tetrahedral clusters promotes crystallization by suppressing five- and seven-membered rings that hinder the emergence of the ordered structure. We also find that slow annealing promotes a bias toward the cubic polymorph relative to the hexagonal counterpart. Finally, we calculate the photonic band structures, showing that the cubic polymorph exhibits a complete photonic band gap for the dielectric filling fraction directly realizable from the designer triblock patchy particles. Unexpectedly, we find that the hexagonal polymorph also supports a complete photonic band gap, albeit only for an increased filling fraction, which can be realized *via* postassembly processing.**

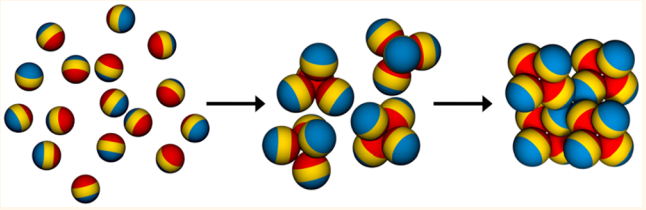

KEYWORDS: *colloidal self-assembly, patchy particles, hierarchical self-assembly, photonic crystals, tetrastack lattice*

Photonic crystals have long served as attractive targets for programmed self-assembly of colloidal particles.[1−3] Colloidal particles are particularly appealing building blocks for bottom-up routes to photonic crystals because their size is comparable to the wavelength of visible light, and the interactions between them can be tuned to program their self-assembly.[4,5] Photonic crystals are periodically structured optical media generally with a photonic band gap (PBG), corresponding to a range of frequencies for photons prohibited to propagate through these media.[6] Of the limited number of three-dimensional (3D) crystals known to have a complete photonic band gap, cubic diamond and cubic tetrastack are especially sought after as they require a relatively low refractive index contrast for the band gap to emerge.[3,7,8] These 3D crystals have rather open structures, making them elusive for being realized *via* bottom-up routes.[9−11]

Programming self-assembly of colloidal particles into open crystals has proved a long-standing challenge due to their mechanical instability for being sparsely populated.[12] For example, the tetrastack lattice is a Maxwell lattice with a mean coordination number that only equals twice the spatial dimension,[13] thus leaving it on the verge of mechanical instability for particles with central-force nearest-neighbor interactions,[14] as per Maxwell's argument.[15] For a bottom-up route to be a viable means of fabrication of a desired colloidal open crystal, the target structure is required to be not only thermodynamically favored for the building blocks of choice but also kinetically accessible *via* self-assembly pathways in preference to metastable structures.[16−18] In the context of self-assembly of tetrahedral patchy particles into a diamond crystal,

Received: October 4, 2019
Accepted: April 22, 2020
Published: May 6, 2020

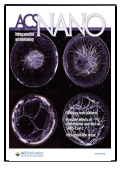

https://dx.doi.org/10.1021/acsnano.9b07849
ACS Nano 2020, 14, 5348−5359

kinetic traps are known to arise from the competition from an amorphous phase with random tetrahedral network structures.[19] The presence of competing cubic and hexagonal polymorphs adds up to the challenge of realizing these colloidal crystals *via* self-assembly pathways for photonic applications.[20−22]

In recent years, triblock patchy particles, spherical in shape with two symmetric patches on the poles separated by a charged band in the middle, emerged as promising building blocks for bottom-up routes to colloidal open crystals. In particular, triblock patchy particles were synthesized with equal-size patches on the poles, and a kagome lattice was self-assembled from these patchy particles in a quasi-two-dimensional system.[23] Subsequently, a computational study, which employed the Kern−Frenkel model for patchy particles,[24] captured the self-assembly of the triblock patchy particles into a kagome lattice and predicted the formation of the close-packed hexagonal lattice at higher pressures.[25] An analytical theory based on lattice dynamics attributed the mechanical stability of the kagome lattice to rotational entropy, whereas its selection over the close-packed hexagonal lattice was attributed to vibrational entropy.[14]

This theoretical framework, when extended to 3D lattices formed by triblock patchy particles, predicted a mixed phase of cubic and hexagonal tetrastack lattices in the region of the phase diagram appropriate for selection of an open lattice over the close-packed counterpart.[14,26] However, the selection between cubic and hexagonal tetrastack crystal structures is assumed to be of paramount importance in the context of photonic applications as only the cubic polymorph has hitherto been known to support a complete PBG.[20,21] In a recent computational study, a cubic tetrastack lattice was selectively self-assembled from triblock patchy particles with staggered triangular patches rather than the conventional circular patches on the poles, using a patterning symmetry concept.[20] More recently, a hexagonal tetrastack lattice was also selectively self-assembled *in silico* by introducing large star polymers commensurate with the void symmetry, thus providing an entropic control.[21] In the latter case, the star polymers act as structure-directing agents to entropically bias the formation of the hexagonal tetrastack lattice, which has a different arrangement of octahedral and tetrahedral voids as compared to its cubic counterpart. Although these computational studies have greatly advanced our fundamental understanding, the design principles have so far proven elusive from the perspective of experimental realizations. The patterning symmetry concept poses the challenge of fabricating patch geometry to a level of sophistication still beyond routine experimental protocols;[20] the use of a structure-directing agent, if not optimal, could destabilize the open crystals relative to their closed-packed counterparts.[21]

In the present work, we conceive of a bottom-up route to tetrastack lattices, exploiting hierarchical self-assembly pathways[27−29] for designer triblock patchy particles and explore whether such pathways promote crystallization or polymorph selection. A tetrastack lattice comprises vertex-shared tetrahedra[2,8] and can thus be envisaged to be realized by a two-stage self-assembly of designer colloidal particles *via* tetrahedral clusters. The key to the success of such a staged assembly scheme to yield a crystal is the self-limiting formation of tetrahedral clusters in the first stage, thus avoiding polydispersity in the second stage. By "self-limiting", it is meant that, over a certain temperature interval, the clusters cease to grow beyond a specific finite size in the first stage of self-assembly, thereby producing uniform secondary building blocks, which can potentially form structures at larger length scales through the second stage of self-assembly.[28,30]

To this end, we built on our recent work, which established a generic design principle to program a hierarchical self-assembly scheme for triblock patchy particles into colloidal open crystals *via* uniform clusters.[31] The triblock patchy particles considered here are modeled after those synthesized recently in the micron scale.[32] A hierarchy of patch−patch interaction strengths encodes a staged self-assembly scheme upon cooling,[18] and the width of the patches and the range over which the patches interact are chosen to satisfy a geometric criterion, also crucial for self-limiting cluster formation. Here, two quite different temperature windows control the assembly process: (i) a broad temperature window at which the particles form tetrahedral clusters and (ii) a much narrower window at lower temperatures where the previously formed tetrahedral clusters aggregate. The uniform secondary building blocks generated by the first stage of self-assembly that occurs over the broad temperature window are thermodynamically stable. These secondary building blocks then form structures at larger length scales through the second stage of self-assembly, which is activated by a further decrease in the temperature. We also present the photonic band structures of both the cubic and hexagonal polymorphs that we find for our designer triblock patchy particles.

RESULTS AND DISCUSSION

We initially employed the basin-hopping algorithm for global optimization on crystal energy landscapes to predict the crystal structures for the triblock patchy particles considered here in search of the parameter space that could possibly support tetrastack crystals. The triblock patchy particles are spherical in shape with two circular patches A and B at opposite poles and modeled as rigid bodies. The effective potential has an isotropic component given by the Yukawa potential that describes screened electrostatic repulsion and an anisotropic component, describing the directional interactions between the circular patches. The details of the effective potential are provided in the Methods section. Here, we only note that we present results using reduced units, with the parameter σ, which appears in the Yukawa potential, taken as the unit of length and the Yukawa contact potential ε_Y as the unit of energy. In the present study, we restricted ourselves to the triblock patchy particles that have two equal-size patches on the poles. The size of the patches was chosen so that each patch could make contacts with three other patches in order to form a tetrahedron, as shown in Figure 1a. We considered such triblock patchy particles of two types: one type has two identical A patches, interacting with a strength $\varepsilon_{AA} = 1$ so that the triblock patchy particles retain the head−tail symmetry in addition to the cylindrical symmetry; the second type involves two different patches, A and B, having different strengths for the interactions between patches such that $\varepsilon_{BB} = 0.2\varepsilon_{AA} = 1$. For simplicity, we fix $\varepsilon_{AB} = \sqrt{\varepsilon_{AA}\varepsilon_{BB}}$. We call the former AA-triblock patchy particles and the latter AB-triblock patchy particles, the latter lacking the head−tail symmetry despite having the patches of the same size.

Figure 1b shows characteristic 16-particle motifs of the two polymorphs that we identify as the global minima on the crystal energy landscape for our designer AB-triblock patchy

https://dx.doi.org/10.1021/acsnano.9b07849
ACS Nano 2020, 14, 5348−5359

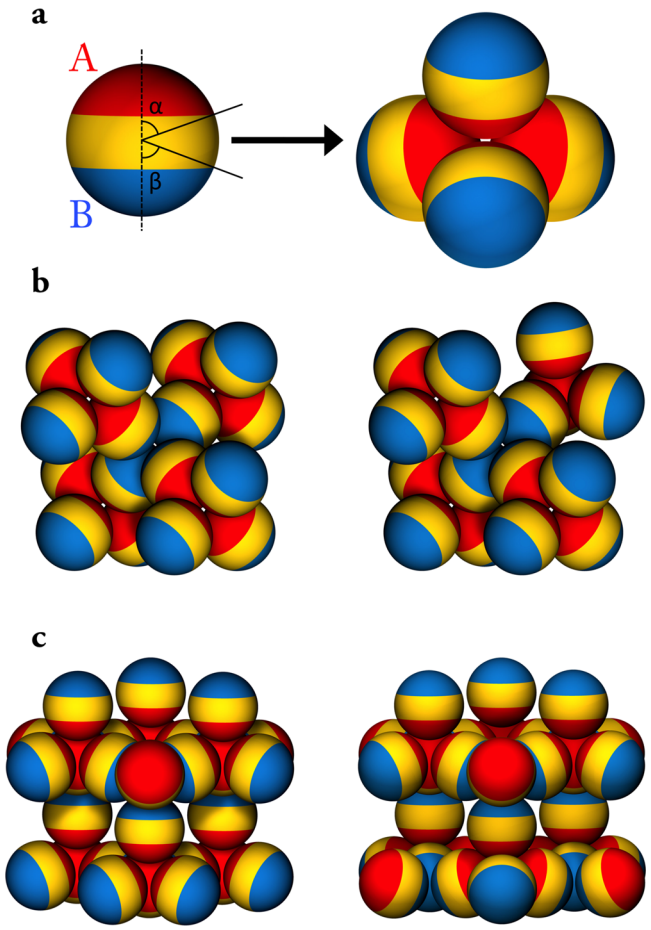

Figure 1. Tetrastack crystal structures formed by triblock patchy particles *via* tetrahedra in the presence of a hierarchy of interactions. (a) Designer triblock patchy particles with equal-size patches on the poles, forming a tetrahedron. Patch A, colored red, forms stronger contacts relative to those formed by patch B, colored blue. (b) Characteristic 16-particle motifs of the cubic (left) and hexagonal (right) tetrastack structures. In the cubic tetrastack structure, each of the four strongly bound tetrahedra formed by A patches are staggered relative to the weakly bound tetrahedron formed by B patches. In the hexagonal polymorph, one of the four strongly bound tetrahedra is in an eclipsed arrangement relative to the weakly bound tetrahedron, and the remaining three are staggered. (c) Portrayal of the cubic and hexagonal tetrastack structures formed by the triblock patchy particles under consideration, highlighting that both of these polymorphs consist of alternating layers of two-dimensional kagome and triangular planes.

particles for a range of parameters. The global minima of the AA-triblock patchy particles are similar to those found for the AB ones. It is noteworthy that the lattices formed by the AB-triblock patchy particles have two distinct sets of tetrahedra, one strongly bound and the other relatively weakly bound, of slightly different volumes. The two polymorphs, both comprising vertex-shared tetrahedra, differ in the relative arrangements of the tetrahedra, as apparent in Figure 1b. In the cubic polymorph, all four strongly bound tetrahedra are staggered relative to the weakly bound tetrahedron formed by the interactions between B patches. On the contrary, only three of the four strongly bound tetrahedra are staggered relative to the weakly bound tetrahedron in the hexagonal polymorph, the fourth one being in an eclipsed arrangement.

Figure 1c presents an alternative view of the two polymorphs, highlighting that both of these polymorphs consist of alternating layers of two-dimensional (2D) kagome and triangular planes. The stacking of successive triangular planes in the cubic polymorph follows the ABCABC sequence observed for the cubic close packing; in the hexagonal polymorph, the stacking instead follows the ABABAB sequence observed in the case of the hexagonal close packing. These stacking sequences are apparent in alternative views, shown in Supporting Figure S1. The cubic polymorph has the space group $F\bar{4}3m$, whereas the space group of the hexagonal polymorph is $P6_3mc$. In contrast, the corresponding counterparts obtained with the AA-triblock patchy particles have the space groups $Fd\bar{3}m$ and $P6_3/mmc$, respectively. The polymorphs for the AB-triblock patchy particles thus lack the inversion symmetry and, strictly speaking, share the space groups with zinc blende and wurtzite rather than cubic and hexagonal diamond, respectively. In the hard-sphere limit for the interactions between the spherical cores, approached by large values of the inverse Debye length, this distinction between the lattices stabilized by the AB- and AA-triblock patchy particles will vanish. We refer to the cubic and hexagonal polymorphs stable for the AB-triblock patchy particles as the cubic and hexagonal tetrastack, not withstanding this distinction, and hereafter denote as CT and HT, respectively, for brevity.

The polymorphs, CT and HT, have identical lattice energies. Our free-energy calculations reveal that the cubic polymorph is marginally more stable compared to the hexagonal polymorph, as evident in Supporting Figure S2. This is in line with what has been reported in the case of the closely related Kern–Frenkel model, for which the CT polymorph has also been found to be more stable than the HT polymorph on the free energy landscape.[33] We, however, note that the free-energy difference between the polymorphs in the present case is rather small, presumably due to smaller contributions to the rotational entropy because of restricted rotational fluctuations arising from the curvature of the potential well here as compared to the Kern–Frenkel potential.

In order to assess the prospect of the CT and HT structures self-assembled from our designer triblock patchy particles, we carried out a series of five independent virtual-move Monte Carlo (VMMC) simulations of the AB-triblock patchy particles at a volume fraction of $\phi = 0.811\phi_T = 0.3$, where $\phi_T = 0.37$ and is the packing fraction of the ideal tetrastack crystals composed of touching spheres. Figure 2a shows how the number of tetrahedra formed, N_{Td}, changes with the temperature, T^*, along with the corresponding change in the average potential energy per particle, U^*/N, for a system of $N = 500$ particles subject to gradual cooling in a representative sequence of simulation runs. The number of tetrahedral clusters present in the system gradually grows over a rather wide range of temperatures as the energetic stability of the tetrahedral clusters driven by the interactions between the stronger patches increasingly outweigh the loss of entropy associated with the formation of the tetrahedral clusters. Over a range of intermediate temperatures, the tetrahedral clusters, however, remain self-limiting due to thermodynamic reason because the weaker patches do not provide enough energetic driving force for further assembly to occur. A near 100% yield of tetrahedral clusters is observed at $T^* = 0.2$ in terms of self-limiting tetrahedra, effectively signaling the completion of the

https://dx.doi.org/10.1021/acsnano.9b07849
ACS Nano 2020, 14, 5348–5359

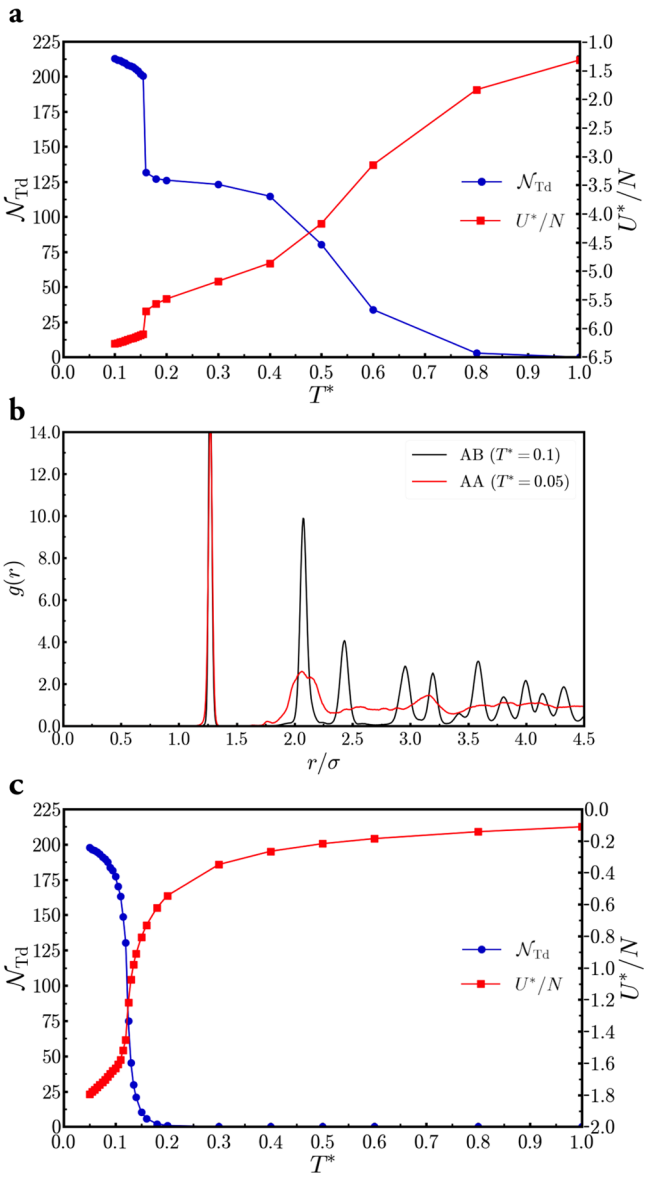

Figure 2. Self-assembly of triblock patchy particles. (a) Two-stage self-assembly of AB-triblock patchy particles into a crystalline structure *via* the formation of tetrahedra. (b) Pair distribution functions $g(r)$ for the centers of the tetrahedra formed by the AB-triblock and AA-triblock patchy particles at representative temperatures. (c) Self-assembly of AA-triblock patchy particles into an amorphous phase. In (a) and (c), the average potential energy per particle and the number of tetrahedral clusters formed, $\mathcal{N}_{Td}$, are shown on two different scales, as a function of the temperature T^* for a system of N = 500 AB-triblock patchy particles and AA-triblock patchy particles, respectively, at the volume fraction ϕ = 0.3 as observed in virtual-move Monte Carlo simulations.

first stage of assembly driven by the stronger patch−patch interactions.

When subjected to further cooling, the average energy per particle is observed to change sharply around T^* = 0.155 when the number of tetrahedral clusters present in the system rises sharply, signaling a first-order phase transition. The pair distribution function calculated for the centers of the tetrahedra confirmed the emergence of long-range correlations, as evident in Figure 2b. Visual inspection of the system confirmed that this structural transition was driven by weaker patch−patch (B−B) interactions, leading to emergent tetrahedra as the discrete tetrahedral clusters organized themselves and thus formed an extended periodic structure of vertex-shared tetrahedra. This scenario is in contrast with what is observed for a system of N = 500 AA-triblock patchy particles, when the system was subject to gradual cooling. For the system of AA-triblock patchy particles, such long-range correlations are absent from the pair distribution function even at a low temperature (see in Figure 2b). However, a significant increase in the growth of the number of tetrahedra present in the system is also observed for the AA-triblock patchy particles across a narrow temperature window, as evident in Figure 2c.

A pertinent question is then what promotes crystallization along the two-stage self-assembly pathways observed in the present case. It is of interest to note that both AA- and AB-triblock patchy particles lead to the formation of a comparable number of tetrahedra at low temperatures (see Figure 2a,c). We identify, by visual inspection, five- and seven-membered rings in representative low-temperature configurations for the system of AA-triblock patchy particles in addition to six- and eight-membered rings present in the perfect lattices. For example, see Supporting Figure S3 for representative low-temperature configurations obtained for AB- and AA-triblock patchy particles. This observation is supported by the quantitative picture presented in Figure 3a, which provides the numbers of rings (four-membered to eight-membered) present, on average, in the configurations at the lowest temperatures investigated for the 500-particle systems studied in VMMC simulations for both AA- and AB-triblock patchy particles using a graph theoretical approach. The six- and eight-membered rings, necessary to form a perfect tetrastack lattice, are shown in Figure 3b,c, respectively, for example. It is noteworthy that five- and seven-membered rings are known to occur in other amorphous materials involving tetrahedral bonding, in line with the random network theory of glasses.[34,35] For example, amorphous silicon contains five- and seven-membered rings in addition to six-membered rings present in the perfect crystal.[36]

It is evident that five- and seven-membered rings are essentially missing in the AB-triblock patchy particle system. A hierarchical self-assembly pathway for the AB-triblock patchy particles proceeds in stages, as also confirmed in our Brownian dynamics (BD) simulations, discussed later. Each strongly bound tetrahedron can already incorporate two vertices of a ring. As a result, the association of tetrahedra *via* the BB bonds produces clusters composed of an even number of vertices. A cluster of three bonded tetrahedra can result in a ring of six bonded vertices. Similarly, a cluster of four bonded tetrahedra can result in a ring of eight bonded vertices. Five- and seven-membered rings are unlikely to form starting from strongly bound tetrahedra, each contributing two vertices, as opposed to single particles. The low-level presence of seven-membered rings, apparent also in Supporting Figure S4, showing the ring statistics at low temperatures, is presumably due to fluctuations around the weak bonds that the strongly bound tetrahedra form through the second stage of assembly. A two-stage self-assembly pathway in this case thus suppresses the formation of five- and seven-membered rings in the second stage of assembly, preventing network defects (in the form of odd membered rings), thus promoting the emergence of long-range order.

https://dx.doi.org/10.1021/acsnano.9b07849
ACS Nano 2020, 14, 5348−5359

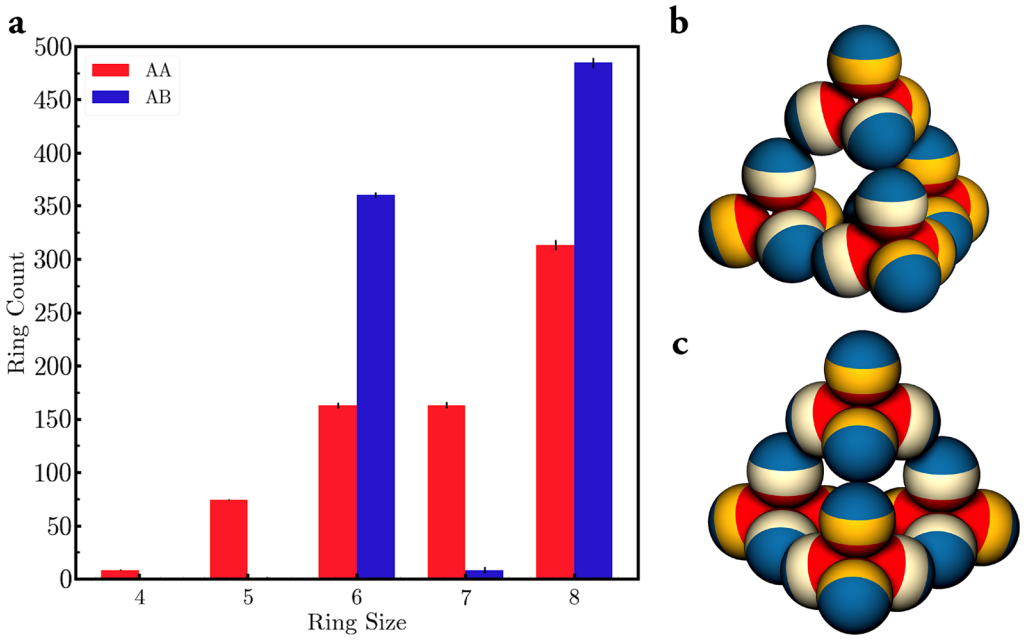

Figure 3. Root of promotion of crystallization *via* hierarchical self-assembly pathways. (a) Counts of rings of different sizes present in a low-temperature configuration on average with error bars for AB- and AA-triblock patchy particles for comparison. The analysis was performed with configurations sampled along the virtual-move Monte Carlo trajectories at the temperatures of $T^* = 0.1$ and $T^* = 0.05$ for $N = 500$ AB- and AA-triblock patchy particles, respectively. (b,c) Two views of the conventional unit cell of the perfect cubic tetrastack, illustrating the presence of six-membered and eight-membered rings. The middle bands of the triblock patchy particles forming a six-membered ring (b) and an eight-membered ring (b) are shown in a lighter shade (*i.e.*, in cream color as opposed to yellow).

It is imperative to have quantitative estimates of the fractions of particles in the cubic and hexagonal environments as stacking hybrids are anticipated in the presence of competing polymorphs. We present here the results of an analysis that considers each particle as a candidate likely to be in a crystalline environment if it has exactly six neighbors and then labels each particle to be in a cubic or a hexagonal or an interfacial environment or leaves it unlabeled, as described in the Methods section. The analysis is based on the characterization of the local environment in terms of the Steinhardt bond-orientational order parameters q_4 and q_6; see Supporting Figure S5 for further details. In order to have a larger sample size, for each independent sequence of runs, 5 million VMMC steps were carried out at $T^* = 0.2$, at which the first stage of assembly is effectively complete, and four configurations, a million VMMC steps apart along the trajectory, were chosen to be subject to further cooling. We thus have four batches of simulation runs below $T^* = 0.2$ for the system of AB-triblock patchy particles, each batch having five independent runs. Below $T^* = 0.2$, all of the simulation runs followed identical annealing protocols. Further details on the annealing protocols are provided in Supporting Information.

Figure 4 shows the fractions of particles labeled as crystalline, cubic, and hexagonal as a function of temperature for different annealing protocols followed for the system through the second stage of assembly. Here, crystalline particles refer to those labeled as cubic or hexagonal or interfacial. It is noteworthy that the annealing protocol is known to play a particularly significant role in achieving high yield for colloidal crystals self-assembled from DNA-coated colloids.[37] Here, the annealing protocols differ across the batches of simulation runs in terms of number of VMMC steps performed at $T^* = 0.2$, where the first stage of assembly is practically complete. It is apparent that the fraction of crystalline particles is significantly higher than the fraction of particles either in the cubic or in the hexagonal environment for the fastest annealing carried out. This implies the presence of a considerable fraction of interfacial particles, which are confined to the kagome planes. Notably, we find that the fraction of particles in the cubic environment gradually grows, and that in the hexagonal environment falls as the annealing becomes slower, though overall crystallinity remains practically unchanged. We therefore infer that the CT polymorph, which is marginally more stable than the HT polymorph, is the thermodynamically controlled product in this case. It is of interest to also note that, for hard spheres, the face-centered cubic (fcc) crystal is only marginally more stable than the hexagonal close-packed (hcp) crystal.[38] In fact, experimental results suggest that slowly grown crystallites display a greater proportion of fcc than hcp,[39] which correlates well with the observations we have made here.[39]

In order to investigate the pathways for crystallization in further detail, we performed a set of three independent BD simulations for a system of $N = 864$ AB-triblock patchy particles, using a relatively gradual annealing protocol. The BD trajectories unequivocally demonstrate that the hierarchical self-assembly proceeds in stages *via* self-limiting tetrahedral clusters. Figure 5a–c shows how the fractions of particles locally in the cubic or hexagonal or interfacial tetrastack environment evolve with time along the three BD trajectories at $T^* = 0.15$, where we observe crystallization upon cooling. The figures show that the cubic component dominates over the hexagonal component for all three trajectories, in line with the expectation for a gradual annealing protocol. We note that, in the case of the second trajectory, the growth of the crystalline environment is more gradual (see Figure 5b) relative to the other two, also evident in the growth of the largest crystalline cluster along each of these dynamical

https://dx.doi.org/10.1021/acsnano.9b07849
ACS Nano 2020, 14, 5348–5359

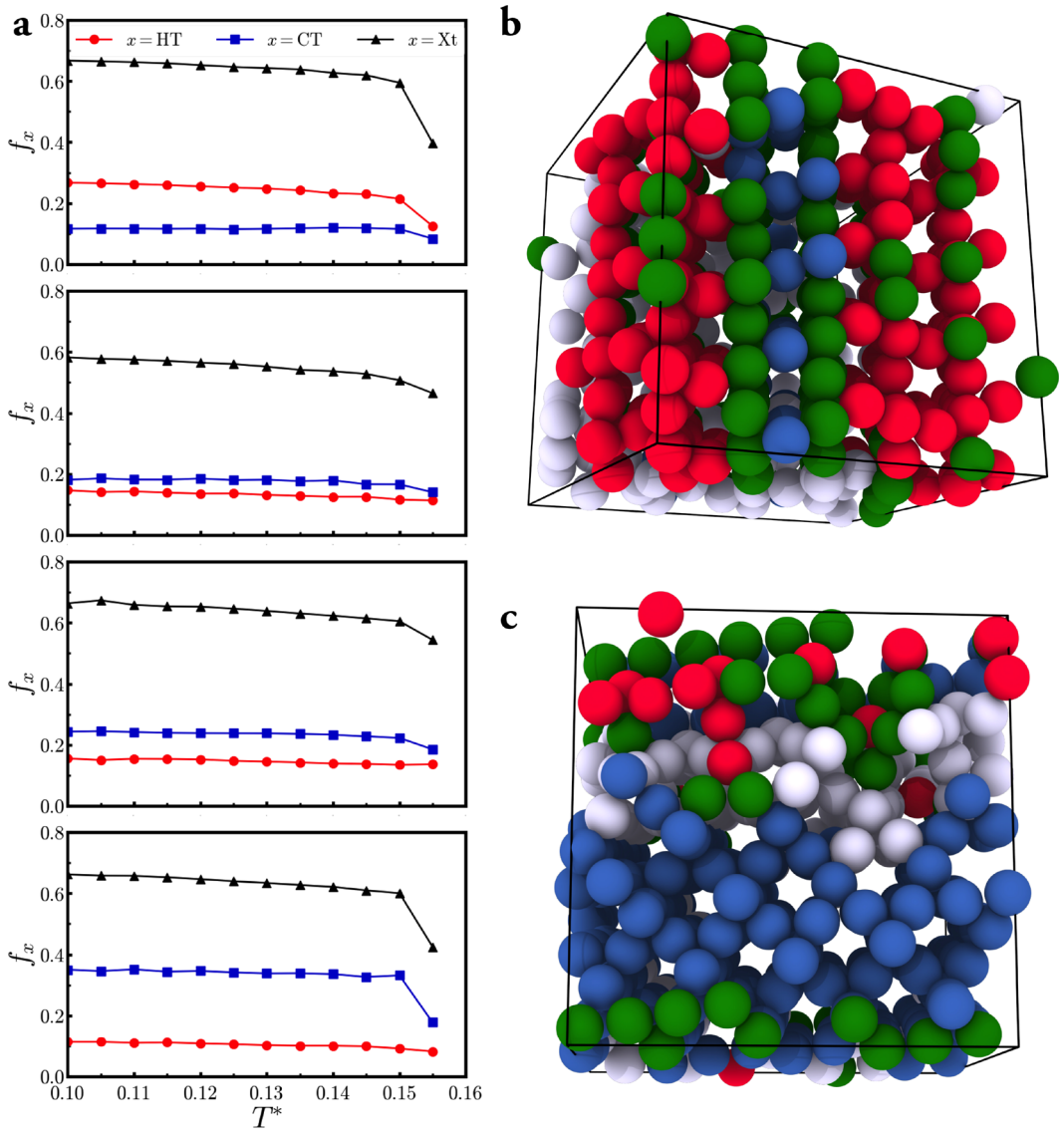

Figure 4. Contents of cubic and hexagonal polymorphs in the mixed tetrastack crystals obtained under different annealing protocols. (a) Fractions of particles locally in crystalline (black lines), cubic (blue lines), and hexagonal (red lines) environments in a system of N = 500 AB-triblock patchy particles studied by virtual-move Monte Carlo simulations as the temperature was gradually reduced following different annealing protocols. From the top to the bottom panels, the system was subject to increasingly large number of Monte Carlo cycles at T^* = 0.2 without any noticeable change in the average energy per particle. (b,c) Snapshots of representative configurations obtained at T^* = 0.1 through the fastest (b) and slowest (c) annealing protocols followed, with the particles color-coded to distinguish their local environments: cubic (blue), hexagonal (red), and interfacial (green). The two configurations are so chosen to highlight their relatively high contents of particles in the hexagonal and cubic environments.

trajectories shown in Supporting Figure S6. Figure 5d–f shows the time evolution of the ring statistics along these trajectories. It is clearly evident that the formation of the six- and eight-membered rings mirrors the growth of the crystalline environment, thus highlighting the importance of the former in the emergence of long-range order. A measure of crystalline yield can be obtained from the sum of the fractions of cubic, hexagonal, and interfacial contents. It appears that the crystalline yields along the BD trajectories are somewhat low compared to what we obtained from our VMMC simulations, and we notice the presence of a larger proportion of seven-membered rings. Along the dynamical trajectories, the seven-membered rings may have formed also due to the presence of some primary particles as a result of the first stage of assembly remaining incomplete in BD simulations.

It is well-established that the cubic tetrastack crystal possesses a complete photonic band gap between the second and third bands.[2,8,22,40−42] However, to the best of our knowledge, the photonic properties of the hexagonal tetrastack crystal have not previously been reported. Moreover, the cubic and hexagonal tetrastack crystals formed by the AB-triblock patchy particles under consideration do not possess the inversion symmetry; they share space groups with zinc blende and wurtzite, rather than cubic and hexagonal diamond, respectively. We therefore investigated the photonic band structures of the cubic and hexagonal polymorphs supported by our designer AB-triblock patchy particles.

The photonic band structures of the cubic and hexagonal tetrastack crystals, as supported by our designer AB-triblock patchy particles, are shown in Figure 6a,b, respectively. We

https://dx.doi.org/10.1021/acsnano.9b07849
ACS Nano 2020, 14, 5348−5359

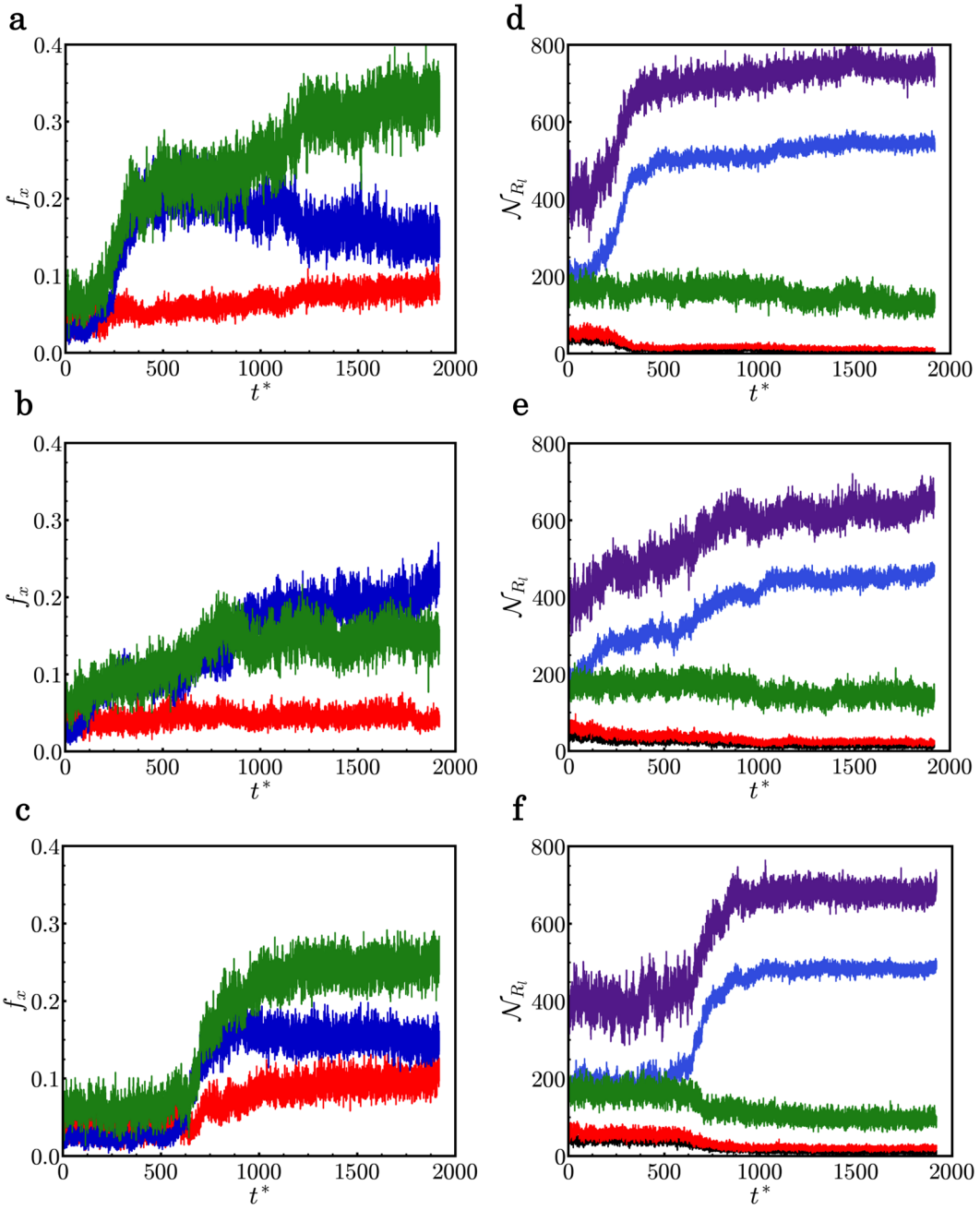

Figure 5. Growth of cubic, hexagonal, and interfacial tetrastack environments and evolution of ring statistics along independent crystallization pathways. (a−c) Evolution of the fractions of particles locally in cubic (blue), hexagonal (red), or interfacial (green) tetrastack environments with time in a system of N = 864 AB-triblock patchy particles along three independent Brownian dynamics trajectories at T^* = 0.15. (d−f) Evolution of the ring statistics with time along the corresponding trajectories. $\mathcal{N}_{R_l}$ is the number of rings of size l present in the system at an instant of time. Four-, five-, six-, seven-, and eight-membered rings, shown in black, red, blue, green, and violet lines, respectively, are identified. The observation time t is set to zero at the instant of reducing the temperature to T^* = 0.15.

present here the results for the direct structures, consisting of high-dielectric spheres embedded in air, corresponding to the ratio r/a = 0.171, where r is the radius of the spheres and a is the lattice constant for the conventional unit cell of the cubic tetrastack structure, as predicted for the set of parameters under consideration here. The r/a ratio thus provides a measure of the dielectric filling fraction. For our calculations, we set the dielectric contrast to be 12 in order to allow for comparison with previous studies.[22,40,41] As customary, the results are shown in terms of the dimensionless frequency $\omega a/2\pi c$, where ω is the frequency of the electromagnetic field and c is the vacuum speed of light.

We find that, for the ratio r/a = 0.171, the cubic tetrastack structure indeed has a complete PBG with a ratio between the band gap and midgap frequencies, $\Delta\omega/\omega_m$, of 4.89%, whereas the hexagonal tetrastack structure does not possess a PBG. Surprisingly, we observe that for a range of r/a values higher than r/a = 0.171, there exists a complete PBG between the fourth and fifth bands even for the hexagonal polymorph, as shown in Figure 6c.

https://dx.doi.org/10.1021/acsnano.9b07849
ACS Nano 2020, 14, 5348−5359

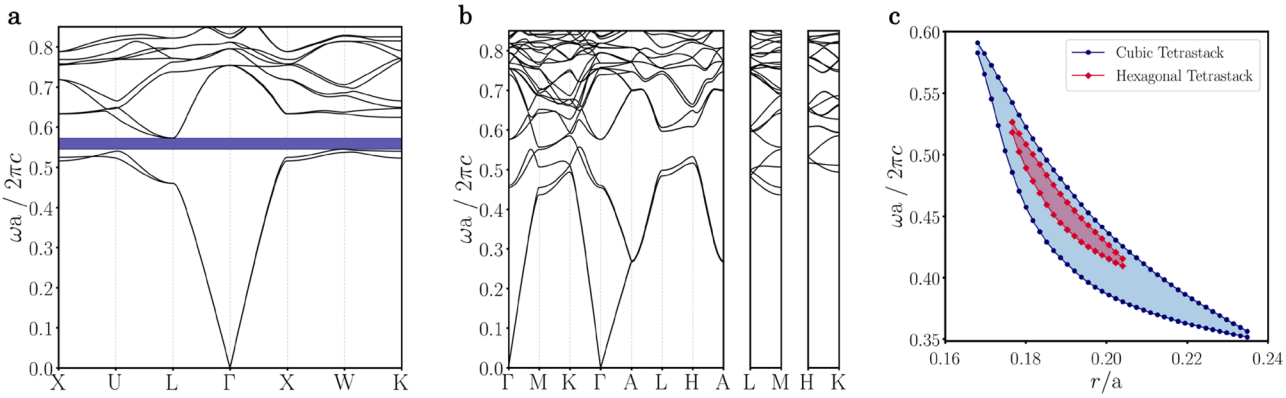

Figure 6. Photonic band structures and band gap maps for the cubic and hexagonal tetrastack structures supported by the AB-triblock patchy particles. Photonic band structures calculated at a dielectric contrast value of 12 for the cubic (a) and hexagonal (b) polymorph. (c) Photonic band gap maps as a function of r/a, where r is the radius of the spheres of the particles and a is the lattice constant of the conventional unit cell of the cubic tetrastack structure as predicted for the set of parameters considered here.

Moreover, the PBGs for both the cubic and hexagonal polymorphs reach a peak of 14.45 and 5.23%, respectively, at the same ratio of r/a = 0.187; the corresponding photonic band structures are shown in Supporting Figure S7. As evident in Figure 6c, the range of the ratio r/a for which the hexagonal tetrastack structure displays a complete PBG is significantly narrower than that of the cubic tetrastack. We note that the r/a ratio that maximizes the complete PBG of the tetrastack crystal structures or supports a complete PBG for the hexagonal polymorph can be realized with our designer triblock patchy particles only *via* postprocessing, which involves depositing more material onto the surface of the particles postassembly, thus increasing the dielectric filling fraction of these structures.[42,43]

The inverse cubic tetrastack structure has a significantly wider complete PBG (26.36% at the peak) than its direct counterpart, as apparent from the photonic band gap maps of the inverse structures presented in Supporting Figure S8. Notably, this is not also the case for the hexagonal polymorph as the inverse hexagonal tetrastack structure displays a relatively narrow complete PBG of 3.15% at the peak. We note that a wide range of sphere radii relative to the lattice constants supports a complete PBG for both polymorphs in their direct as well as inverse structures, and the PBGs spectrally overlap.

We studied the sensitivity of the relative gap width of the photonic band gap, $\Delta\omega/\omega_m$, as a function of the $\varepsilon_{AA}/\varepsilon_{BB}$ ratio for the cubic polymorph. We note that changing the $\varepsilon_{AA}/\varepsilon_{BB}$ ratio does not produce a photonic band gap in the hexagonal polymorph. We find that the relative gap width increases as the $\varepsilon_{AA}/\varepsilon_{BB}$ ratio increases, with ε_{BB} set to unity, as shown in Supporting Figure S9. This trend appears to be along the line expected from the consideration that the volume of the voids inside the strongly bound tetrahedra formed *via* the interaction between A patches decreases as the ratio $\varepsilon_{AA}/\varepsilon_{BB}$ increases. With the particles coming closer together, the periodic structure approaches the limit of a continuous network that would have been formed by touching spheres. It is well-known that network structures are more favorable for the formation of a 3D photonic band gap as the electric field energy in the dielectric band can be better confined to the high-dielectric region, lowering its frequency and increasing the width of the gap.[44]

CONCLUSION

We here employ a hierarchical self-assembly scheme encoded in triblock patchy particles to establish a bottom-up route to tetrastack crystals, which comprise vertex-shared tetrahedra. The hierarchical self-assembly pathways proceed in two stages, forming self-limiting tetrahedra upon completion of the first stage en route to tetrastack crystals. In this assembly scheme, we exploit a hierarchy of patch−patch interactions to induce the staged assembly upon cooling, whereas the formation of self-limiting clusters in the first stage is achieved by the choice of patch size and the range of patch−patch interactions. The use of hierarchy of strengths for patch−patch interactions, controlled by the ratio $\varepsilon_{AA}/\varepsilon_{BB}$, ensures that the assembly driven by the interactions between the two types of patches are well-separated—an aspect also critical to the assemblage being self-limiting in the first stage. In the present study, this ratio was set to equal five, guided by our previous observation that a smaller ratio of two failed to yield a crystal despite the assembly in the first stage being self-limiting.[31] A weaker interaction strength for the patches driving the second stage of assembly ensures reversible bond formation at low temperatures at the expense of thermodynamic driving forces, thus allowing for the kinetic traps arising from the formation of incorrect contacts to be negotiated effectively.[18]

The present work reveals that a hierarchy of interaction strengths is crucial to promote crystallization, even though stable tetrastack crystal structures exist for $\varepsilon_{AA} = \varepsilon_{BB}$. In the context of these crystals being self-assembled, we find that the cubic and hexagonal tetrastack crystal structures are in competition with disordered network structures. Our results demonstrate that the hierarchical self-assembly pathways followed by our designer triblock patchy particles promote the formation of six- and eight-membered rings present in the perfect crystal structures as opposed to five- and seven-membered rings and thus help negotiate the kinetic traps to yield crystals.

Although the hierarchical self-assembly pathways promote crystallization, they do not result in the selection of one or the other polymorph. This result is in line with what is expected from only a marginal free-energy difference between the polymorphs, as confirmed by our free-energy calculations. We obtain a mixed tetrastack crystal with particles in the cubic as well as hexagonal environments. We present an analysis, which assigns the local environment of a particle to be cubic,

https://dx.doi.org/10.1021/acsnano.9b07849
ACS Nano 2020, 14, 5348−5359

hexagonal, or interfacial. Such assignment allows for comparison of the contents of the cubic and hexagonal polymorphs in a mixed tetrastack crystal. We observe that slow annealing promotes the content of the cubic polymorph over that of the hexagonal polymorph. It is noteworthy that the cubic polymorph is known to be thermodynamically more stable, albeit slightly, relative to the hexagonal polymorph also for a closely related model system.[33]

We present the photonic band structures for both the cubic and hexagonal polymorphs of tetrastack crystal. Notably, a complete PBG is found to emerge for the hexagonal polymorph at high dielectric filling fractions realizable experimentally. We also find that the cubic polymorph supports a complete PBG at lower dielectric filling fractions even in the absence of the inversion symmetry.

The AA-triblock patchy particles considered here closely resemble those synthesized in the laboratory.[32] The exploitation of the gold−thiol chemistry for the fabrication of patches, where the thickness of gold coating can be controllably varied to realize van der Waals attractions of different strengths, offers a plausible route to the synthesis of the designer AB-triblock patchy particles.[45,46] The tolerance to polydispersity in the patch width at the level of sophistication achievable in a state-of-the-art experimental fabrication procedure was already established for triblock patchy particles of the AB-type to yield crystals *via* two-stage self-assembly pathways in a previous study.[31] Although the dielectric filling fractions required for realizing an optimal complete PBG in either polymorph can be achieved *via* postprocessing, the issue of selection of one polymorph exclusively *via* such hierarchical self-assembly pathways remains to be addressed.

We finally note in passing that two-stage self-assembly is at the heart of DNA nanotechnology,[47] where properly designed DNA oligomers are mixed together to self-assemble into finite-size bricks. Adding sticky sequences to the sequence design makes it possible also to trigger a secondary self-assembly stage in which the bricks bind to each other.[48] Bricks formed by DNA-made tetravalent particles have been studied experimentally as well as numerically and shown to self-assemble into disordered networks.[49,50]

METHODS

Model. In this work, the traditional one-component description for the colloidal suspensions was considered with a pairwise effective potential.[31,51] As noted previously, the designer triblock patchy colloidal particles are spherical in shape with two circular patches A and B at opposite poles and modeled as rigid bodies. Although patches A and B can differ in terms of their surface coverage, characterized by the angles α and β, respectively, defining their half-patch widths, here, we restrict ourselves to considering triblock patchy particles with equal-size patches at opposite poles (*i.e.*, $\alpha = \beta$). In the present case, patches A and B can both interact with themselves and one another. Here, ε_{AB} is the depth of the potential due to the patch A−patch B interaction when the two patches face each other. The effective potential for a pair of patchy particles U_{ij} is given by

$$U_{ij}(\mathbf{r}_{ij}, \mathbf{\Omega}_i, \mathbf{\Omega}_j) = U_Y(r_{ij}) + \sum_{p\in i}\sum_{p'\in j} U_{pp'}(\mathbf{r}_{ij}, \mathbf{\Omega}_i, \mathbf{\Omega}_j) w_{pp'}(r_{ij}) \quad (1)$$

where $\mathbf{r}_{ij} = \mathbf{r}_j - \mathbf{r}_i$ is the separation vector between triblock patchy particles i and j, $\mathbf{r}_i$ is the position vector for the geometric center of the patchy particle i, and r_{ij} is the magnitude of the vector $\mathbf{r}_{ij}$. $\mathbf{\Omega}_i$ and $\mathbf{\Omega}_j$ describe the orientations of particles i and j, respectively. The isotropic component U_Y is the repulsive Yukawa potential:

$$U_Y(r_{ij}) = \varepsilon_Y \frac{\exp[-\kappa(r_{ij} - \sigma)]}{r_{ij}/\sigma} \quad (2)$$

where κ is the inverse Debye screening length and ε_Y is the Yukawa contact potential.

The angular dependence of the patch−patch interaction is described by $U_{pp'}$:

$$U_{pp'}(\mathbf{r}_{ij}, \mathbf{\Omega}_i, \mathbf{\Omega}_j) = \varepsilon_{pp'}\frac{1}{4}[1 + \Phi(\mathbf{r}_{ij}, \mathbf{\Omega}_i, \mathbf{p}_i)][1 + \Phi(\mathbf{r}_{ji}, \mathbf{\Omega}_j, \mathbf{p}_j)] \quad (3)$$

$$\Phi(\mathbf{r}_{ij}, \mathbf{\Omega}_i, \mathbf{p}_i) = \begin{cases} -1, & \cos\theta_{ijp_i} < \cos\delta \\ -\cos\left(\dfrac{\pi[\cos\theta_{ijp_i} - \cos\delta]}{1 - \cos\delta}\right) & \cos\theta_{ijp_i} \geq \cos\delta \end{cases} \quad (4)$$

Here, $\mathbf{p}_i$ is a normalized vector from the center of the spherical particle i in the direction of the center of patch p on it and thus depends on $\mathbf{\Omega}_i$; $\cos\theta_{ijp_i}$ is the scalar product of the vectors $\hat{\mathbf{r}}_{ij}$ and $\mathbf{p}_i$. Here, $\delta = \alpha,\beta$, and hence, the parameter $\cos\delta$ controls the width of a patch.

The distance dependence of the patch−patch interaction is governed by the function $w_{pp'}$:

$$w_{pp'}(r_{ij}) = \begin{cases} -1, & \text{if } (r_{ij} - \lambda) < 0 \\ -\dfrac{1}{2}[1 + \cos(\pi(r_{ij} - \lambda)s)], & \text{if } 0 \leq (r_{ij} - \lambda) \leq s^{-1} \\ 0, & \text{if } (r_{ij} - \lambda) > s^{-1} \end{cases} \quad (5)$$

where λ is the largest separation at which the patch p−patch p' attraction is at its strongest and the parameter s controls the range over which this attraction vanishes. In the present study, λ was set to 1.01σ. We used reduced units: the length in the units of σ, the energy in the units of ε_Y, the temperature in the units of ε_Y/k_B, with the Boltzmann constant k_B taken to be equal to one. The parameter σ provides an estimate for the size of the charge-stabilized patchy particles in the absence of a hard core.

Crystal Structure Prediction. We identified the global minima on the crystal energy landscapes for triblock patchy particles using the basin-hopping global optimization method, as implemented in the software package GlOSP developed in-house. The implementation in GlOSP, a program for global optimization for structure prediction, follows the prescription of ref 52. In search of both cubic and hexagonal tetrastack structures, we carried out 1 million basin-hopping steps for unit cells containing four and eight patchy particles to allow for tetrahedral motifs.

Upon crystal structure prediction, we considered AA- and AB-triblock patchy particles for the following two sets of parameters for further investigation:

(1) $\varepsilon_{AA} = 1$, $\varepsilon_{BB} = 1$, $\alpha = 80°$, $\beta = 80°$, $\kappa = 100$, $s = 5$;
(2) $\varepsilon_{AA} = 5$, $\varepsilon_{BB} = 1$, $\alpha = 80°$, $\beta = 80°$, $\kappa = 100$, $s = 5$.

It is apparent that the difference in the two sets lies essentially in one parameter, which incorporates a hierarchy of interaction strengths for the patch−patch attractions.

We used the freely available spglib package[53] in order to standardize the unit cell parameters optimized in the basin-hopping runs performed with GlOSP into primitive cell parameters and extract the corresponding fractional coordinates of the particles.

Monte Carlo Simulations. We performed a series of virtual-move Monte Carlo simulations in the canonical ensemble for both AB- and AA-triblock patchy particles, using a system of $N = 500$ particles in each case. A cubic box under periodic boundary conditions was used with the minimum image convention. We employed the symmetrized version of the virtual-move Monte Carlo algorithm,[54,55] implemented in PaSSion, a package for soft matter simulation developed in-house.

https://dx.doi.org/10.1021/acsnano.9b07849
ACS Nano 2020, 14, 5348−5359

The implementation represents the orientational degrees of freedom by quaternions and follows a recent prescription.[56] Each VMMC cycle consisted of N translation or collective rotational cluster moves, chosen at random with equal probabilities. The maximum step size for both the translational and collective rotational cluster moves were fixed, taken as $\delta = 0.1$ in the reduced unit and $\theta_{max} = 0.1$, respectively. The systems were equilibrated from an initial face-centered lattice at $T^* = 1$, and T^* was gradually reduced.

Brownian Dynamics Simulations. We performed a series of Brownian dynamics simulations with $N = 864$ AB-triblock patchy particles contained within a cubic box, using periodic boundary conditions with the minimum image convention. The potential energy was calculated using a spherical cutoff of radius 1.3. The BD simulations were carried out in the overdamped limit, following an algorithm for spherical particles with orientational degrees of freedom represented by a unit vector;[57] hydrodynamic correlations and translation−rotation coupling were ignored. We used appropriate Stokes laws with sticky boundary conditions for the translational and rotational diffusion coefficients at infinite dilution. For our BD simulations, the time was expressed in the units of σ^2/D_0^t, where D_0^t is the translational diffusion coefficient at infinite dilution. The system was equilibrated at $T^* = 1$ from an initial face-centered lattice and three well-separated configurations were chosen to subject them gradual cooling. For each independent run, at each value of T^* studied down to $T^* = 0.5$, the BD trajectory was run for 2×10^7 steps and then for 4×10^7 steps down to $T^* = 0.1525$ and finally for 96×10^7 at $T^* = 0.15$. A time step of $\Delta t = 2 \times 10^{-6}$ in the reduced unit was used for all T^* values studied.

Bond-Orientational Order Parameters. We performed an analysis based on the Steinhardt bond-orientational order parameters q_4 and q_6 for each particle to characterize the local environment.[58,59] In this analysis, each particle i is assigned to have a complex vector $\boldsymbol{q}_l(i)$, with $2l + 1$ components; the mth unnormalized component of $\boldsymbol{q}_l(i)$ is given by

$$q_{lm}(i) = \frac{1}{N_b(i)} \sum_{j=1}^{N_b(i)} Y_{lm}(\hat{\boldsymbol{r}}_{ij}) \tag{6}$$

where $N_b(i)$ is the number of neighbors of particle i located within a distance corresponding to the location of the first peak of the radial distribution function and $Y_{lm}(\hat{\boldsymbol{r}}_{ij}) \equiv Y_{lm}(\theta_{ij},\phi_{ij})$ are the spherical harmonics corresponding to the polar and azimuthal angles, θ_{ij} and ϕ_{ij}, respectively, of the bond $\boldsymbol{r}_{ij}$ between i and its neighbor j. We calculated the Steinhardt bond-orientational order parameter

$$q_l(i) = \sqrt{\frac{4\pi}{2l+1} \sum_{m=-l}^{+l} |q_{lm}(i)|^2} \tag{7}$$

for $l = 4$ and $l = 6$.

Orientational Order Parameter. We used the tetrahedral order parameter, q_{td}, to identify the tetrahedra formed by the particles in a system under consideration. For a cluster of four particles to be a perfect tetrahedron, the tetrahedral order parameter

$$q_{td} = 1 - \frac{3}{8} \sum_{j=1}^{3} \sum_{k=j+1}^{4} \left(\cos \psi_{jk} + \frac{1}{3}\right)^2 \tag{8}$$

where ψ_{jk} is the angle subtended at the center of the cluster by the two vectors joining the center of the cluster to particles j and k; $q_{td} = 1$ in the case of a perfect tetrahedron.[60,61] We identified a set of neighbors for each particle i, using a spatial cutoff r_c for the distance between the centers of the patches facing each other ($r_c = 0.3$). q_{td} was then calculated for all distinct sets of four particles including the selected particle. All sets of four particles satisfying a given threshold for the calculated q_{td} (>0.99) values were considered to form tetrahedra, with measures in place to ensure each set of four particles deemed tetrahedral to be a unique set.

Assignment of Local Environments of Particles. The cubic and hexagonal tetrastack structures both consist of vertex-shared tetrahedra. Each particle sitting at a vertex can be labeled staggered or eclipsed depending upon whether the two tetrahedra it is part of are staggered or eclipsed relative to one another. Both the structures can also be viewed as comprising alternating layers of two-dimensional kagome and triangular planes. The difference between the two structures arises in the relative stacking of the kagome planes, which leaves all the particles in the cubic polymorph as staggered in contrast to only three-quarters in the hexagonal polymorph. The kagome planes in the perfect hexagonal tetrastack crystal along the [001] axis have only staggered particles, each of which has two eclipsed neighbors lying in the triangular planes above and below the kagome plane.

We devised an assignment scheme based on the local environments of the particles in the structure self-assembled from our designer triblock patchy particles. The scheme first identifies whether a particle is in a crystalline environment based on its number of neighbors and then assigns each crystalline particle to be staggered or eclipsed using the calculated values of the Steinhardt bond-orientational parameters q_4 and q_6. If the calculated values do not satisfy certain conditions appropriate for a particle to be labeled as staggered (condition I: $0.32 < q_4 < 0.43$ and $0.65 < q_6 < 0.83$) or eclipsed (condition II: $0.13 < q_4 < 0.23$ and $0.35 < q_6 < 0.47$), the particle is left unlabeled. The eclipsed particles are assigned to be in hexagonal environment, whereas the staggered particles are further classified into cubic, hexagonal, or interfacial environment based on its number of eclipsed neighbors. The scheme is presented in detail with the help of a decision tree shown in Supporting Figure S5.

The ranges of values we used for the bond-orientational order parameters, q_4 and q_6, to label the particles as being in a staggered or eclipsed environment are effectively centered on the corresponding values in the perfect crystal structures. In the perfect cubic tetrastack crystal, we identified all the staggered particles to have the following bond-orientational order parameter values: $q_4 = 0.375$ and $q_6 = 0.741$. However, only three-quarters of the particles in a perfect hexagonal tetrastack crystal are in a staggered environment (with the same set of values for q_4 and q_6), the remaining being in an eclipsed environment. For these eclipsed particles forming the triangular layers along the [001] axis, the bond-orientational order parameter values were found to be $q_4 = 0.181$ and $q_6 = 0.411$.

Photonic Band Structure Calculations. We calculated the photonic band structures of the two polymorphs of tetrastack using the freely available MIT Photonic-Bands (MPB) software package, version 1.7.[62] The MPB software computes fully vectorial eigenmodes of Maxwell's equations with periodic boundary conditions by a preconditioned conjugate-gradient minimization of the block Rayleigh quotient in a plane wave basis. The software takes the fractional coordinates and geometry of the particles, the lattice parameters of the crystal structure and the dielectric contrast as input. The photonic band structure calculations for the cubic and hexagonal tetrastack structures were performed for the 25 lowest energy bands, the former at 307 $\boldsymbol{k}$-vectors with the primitive unit cell discretized on a $32 \times 32 \times 32$ grid and the latter at 462 $\boldsymbol{k}$-vectors with the primitive unit cell discretized on a $32 \times 32 \times 54$ grid. The extra grid points were used in the calculations for the hexagonal polymorph to account for its larger unit cell volume.

Ring Statistics. We calculate the distribution of rings, with lengths $R_l \in [4-8]$, in a system of N particles using a graph-theoretical approach. We describe our patchy particle system as a periodic undirected graph, where each vertex represents a particle center and the edges represent a bond between two particles. We define a cycle as a closed path in this graph (*i.e.*, a path whose first and final vertices are the same). We then define a ring as a cycle that forms part of the minimum cycle basis in our periodic graph. For each vertex in the graph, we calculate all distinct paths with R_l edges using a depth-first search traversal, up to the chosen maximum R_l, making sure to prune paths with edges between nonadjacent vertices and those whose first and last vertices are not the same. This provides us with a count of rings with lengths R_l, of which each vertex is a part.

The ring statistics, shown in Figure 3, are presented by sampling 1000 configurations. The error bars are included in the histograms. It is apparent that the numbers do not fluctuate much.

https://dx.doi.org/10.1021/acsnano.9b07849
ACS Nano 2020, 14, 5348−5359

ASSOCIATED CONTENT

Supporting Information

The Supporting Information is available free of charge at https://pubs.acs.org/doi/10.1021/acsnano.9b07849.

Method of free-energy calculations; detailed annealing protocols; analysis of ring statistics at low temperatures; analysis of crystallization pathways; Figures S1−S9 (PDF)

AUTHOR INFORMATION

Corresponding Author

Dwaipayan Chakrabarti − *School of Chemistry, University of Birmingham, Birmingham B15 2TT, United Kingdom;* orcid.org/0000-0002-2939-2808; Email: d.chakrabarti@bham.ac.uk

Authors

Abhishek B. Rao − *School of Chemistry, University of Birmingham, Birmingham B15 2TT, United Kingdom*

James Shaw − *School of Chemistry, University of Birmingham, Birmingham B15 2TT, United Kingdom*

Andreas Neophytou − *School of Chemistry, University of Birmingham, Birmingham B15 2TT, United Kingdom*

Daniel Morphew − *School of Chemistry, University of Birmingham, Birmingham B15 2TT, United Kingdom*

Francesco Sciortino − *Dipartimento di Fisica, Sapienza Università di Roma, 00185 Roma, Italy;* orcid.org/0000-0002-2418-2713

Roy L. Johnston − *School of Chemistry, University of Birmingham, Birmingham B15 2TT, United Kingdom;* orcid.org/0000-0003-4019-9280

Complete contact information is available at: https://pubs.acs.org/10.1021/acsnano.9b07849

Author Contributions

[§]A.B.R., J.S., and A.N. contributed equally to this work.

Notes

The authors declare no competing financial interest.

ACKNOWLEDGMENTS

We are deeply saddened to report that R.L.J. died on August 16, 2019. A.B.R., J.S., and D.M. gratefully acknowledge support from the Engineering and Physical Sciences Research Council (EPSRC) of the U.K. (Grant No. EP/M506461/1) and the University of Birmingham. F.S. acknowledges support from Ministero dell'Istruzione, dell'Università e della Ricerca (Grant No. PRIN2017-2017Z55KCW). We acknowledge the use of the University of Birmingham's BlueBEAR HPC service and Athena at HPC Midlands+, which was funded by the EPSRC with Grant No. EP/P020232/1, as part of the HPC Midlands+ consortium in this research. A.N., F.S., and D.C. also gratefully acknowledge support of the Royal Society via International Exchanges Award IES\R3\183166. A.N. thanks the Institute of Advanced Studies of the University of Birmingham for support.

REFERENCES

(1) Maldovan, M.; Ullal, C. K.; Carter, W. C.; Thomas, E. L. Exploring for 3D Photonic Bandgap Structures in the 11 F.C.C. Space Groups. *Nat. Mater.* **2003**, *2*, 664−667.

(2) Hynninen, A.-P.; Thijssen, J. H. J.; Vermolen, E. C. M.; Dijkstra, M.; van Blaaderen, A. Self-Assembly Route for Photonic Crystals with a Bandgap in the Visible Region. *Nat. Mater.* **2007**, *6*, 202−205.

(3) Ducrot, E.; He, M.; Yi, G.-R.; Pine, D. J. Colloidal Alloys with Preassembled Clusters and Spheres. *Nat. Mater.* **2017**, *16*, 652−657.

(4) Glotzer, S. C.; Solomon, M. J. Anisotropy of Building Blocks and their Assembly into Complex Structures. *Nat. Mater.* **2007**, *6*, 557.

(5) von Freymann, G.; Kitaev, V.; Lotsch, B. V.; Ozin, G. A. Bottom-Up Assembly of Photonic Crystals. *Chem. Soc. Rev.* **2013**, *42*, 2528−2554.

(6) Joannopoulos, J. D.; Villeneuve, P. R.; Fan, S. Photonic Crystals: Putting a New Twist on Light. *Nature* **1997**, *386*, 143−149.

(7) Ho, K. M.; Chan, C. T.; Soukoulis, C. M. Existence of a Photonic Gap in Periodic Dielectric Structures. *Phys. Rev. Lett.* **1990**, *65*, 3152−3155.

(8) Ngo, T. T.; Liddell, C. M.; Ghebrebrhan, M.; Joannopoulos, J. D. Tetrastack: Colloidal Diamond-Inspired Structure with Omnidirectional Photonic Band Gap for Low Refractive Index Contrast. *Appl. Phys. Lett.* **2006**, *88*, 241920.

(9) Zhang, Z.; Keys, A. S.; Chen, T.; Glotzer, S. C. Self-Assembly of Patchy Particles into Diamond Structures through Molecular Mimicry. *Langmuir* **2005**, *21*, 11547−11551.

(10) Noya, E. G.; Vega, C.; Doye, J. P. K.; Louis, A. A. The Stability of a Crystal with Diamond Structure for Patchy Particles with Tetrahedral Symmetry. *J. Chem. Phys.* **2010**, *132*, 234511.

(11) Romano, F.; Sanz, E.; Sciortino, F. Crystallization of Tetrahedral Patchy Particles *in silico*. *J. Chem. Phys.* **2011**, *134*, 174502.

(12) Cates, M. E. Patchy Colloids: Entropy Stabilizes Open Crystals. *Nat. Mater.* **2013**, *12*, 179−180.

(13) Mao, X.; Lubensky, T. C. Maxwell Lattices and Topological Mechanics. *Annu. Rev. Condens. Matter Phys.* **2018**, *9*, 413−433.

(14) Mao, X.; Chen, Q.; Granick, S. Entropy Favours Open Colloidal Lattices. *Nat. Mater.* **2013**, *12*, 217−222.

(15) Maxwell, J. C. On the Calculation of the Equilibrium and Stiffness of Frames. *Philos. Mag.* **1864**, *27*, 294−299.

(16) Frenkel, D.; Wales, D. J. Colloidal Self-Assembly − Designed to Yield. *Nat. Mater.* **2011**, *10*, 410−411.

(17) Whitelam, S.; Jack, R. L. The Statistical Mechanics of Dynamic Pathways to Self-Assembly. *Annu. Rev. Phys. Chem.* **2015**, *66*, 143.

(18) Morphew, D.; Chakrabarti, D. Programming Hierarchical Self-Assembly of Colloids: Matching Stability and Accessibility. *Nanoscale* **2018**, *10*, 13875−13882.

(19) Smallenburg, F.; Sciortino, F. Liquids More Stable than Crystals in Particles with Limited Valence and Flexible Bonds. *Nat. Phys.* **2013**, *9*, 554−558.

(20) Romano, F.; Sciortino, F. Patterning Symmetry in the Rational Design of Colloidal Crystals. *Nat. Commun.* **2012**, *3*, 975.

(21) Mahynski, N. A.; Rovigatti, L.; Likos, C. N.; Panagiotopoulos, A. Z. Bottom-Up Colloidal Crystal Assembly with a Twist. *ACS Nano* **2016**, *10*, 5459−5467.

(22) Pattabhiraman, H.; Avvisati, G.; Dijkstra, M. Novel Pyrochlore-like Crystal with a Photonic Band Gap Self-Assembled Using Colloids with a Simple Interaction Potential. *Phys. Rev. Lett.* **2017**, *119*, 157504.

(23) Chen, Q.; Bae, S. C.; Granick, S. Directed Self-Assembly of a Colloidal Kagome Lattice. *Nature* **2011**, *469*, 381−384.

(24) Kern, N.; Frenkel, D. Fluid−Fluid Coexistence in Colloidal Systems with Short-Ranged Strongly Directional Attraction. *J. Chem. Phys.* **2003**, *118*, 9882−9889.

(25) Romano, F.; Sciortino, F. Two Dimensional Assembly of Triblock Janus Particles into Crystal Phases in the Two Bond per Patch Limit. *Soft Matter* **2011**, *7*, 5799.

(26) Rocklin, D. Z.; Mao, X. Self-Assembly of Three-Dimensional Open Structures Using Patchy Colloidal Particles. *Soft Matter* **2014**, *10*, 7569−7576.

(27) He, Y.; Ye, T.; Su, M.; Zhang, C.; Ribbe, A. E.; Jiang, W.; Mao, C. Hierarchical Self-Assembly of DNA into Symmetric Supramolecular Polyhedra. *Nature* **2008**, *452*, 198−201.

(28) O'Brien, M. N.; Jones, M. R.; Mirkin, C. A. The Nature and Implications of Uniformity in the Hierarchical Organization of

Nanomaterials. *Proc. Natl. Acad. Sci. U. S. A.* **2016**, *113*, 11717−11725.
(29) Chandrasekaran, A. R.; Zhuo, R. A 'Tile' Tale: Hierarchical Self-Assembly of DNA Lattices. *Appl. Mater. Today* **2016**, *2*, 7−16.
(30) Nguyen, T. D.; Schultz, B. A.; Kotov, N. A.; Glotzer, S. C. Generic, Phenomenological, On-the-Fly Renormalized Repulsion Model for Self-Limited Organization of Terminal Supraparticle Assemblies. *Proc. Natl. Acad. Sci. U. S. A.* **2015**, *112*, E3161−E3168.
(31) Morphew, D.; Shaw, J.; Avins, C.; Chakrabarti, D. Programming Hierarchical Self-Assembly of Patchy Particles into Colloidal Crystals *via* Colloidal Molecules. *ACS Nano* **2018**, *12*, 2355−2364.
(32) Chen, Q.; Bae, S. C.; Granick, S. Staged Self-Assembly of Colloidal Metastructures. *J. Am. Chem. Soc.* **2012**, *134*, 11080−11083.
(33) Reinhart, W. F.; Panagiotopoulos, A. Z. Equilibrium Crystal Phases of Triblock Janus Colloids. *J. Chem. Phys.* **2016**, *145*, 094505.
(34) Zachariasen, W. H. The Atomic Arrangement in Glass. *J. Am. Chem. Soc.* **1932**, *54*, 3841−3851.
(35) Saika-Voivod, I.; Smallenburg, F.; Sciortino, F. Understanding Tetrahedral Liquids through Patchy Colloids. *J. Chem. Phys.* **2013**, *139*, 234901.
(36) Opletal, G.; Petersen, T. C.; Snook, I. K.; McCulloch, D. G. Modeling of Structure and Porosity in Amorphous Silicon Systems Using Monte Carlo Methods. *J. Chem. Phys.* **2007**, *126*, 214705.
(37) Rogers, W. B.; Shih, W. M.; Manoharan, V. N. Using DNA to Program the Self-Assembly of Colloidal Nanoparticles and Microparticles. *Nat. Rev. Mater.* **2016**, *1*, 364−368.
(38) Bolhuis, P. B.; Frenkel, D.; Mau, S.; Huse, D. Entropy Difference between Crystal Phases. *Nature* **1997**, *388*, 235−236.
(39) Pusey, P. N.; Van Megen, W.; Bartlett, P.; Ackerson, B. J.; Rarity, J. G.; Underwood, S. M. Structure of Crystals of Hard Colloidal Spheres. *Phys. Rev. Lett.* **1989**, *63*, 2753.
(40) Garcia-Adeva, A. J. Band Gap Atlas for Photonic Crystals Having the Symmetry of the Kagome and Pyrochlore Lattices. *New J. Phys.* **2006**, *8*, 86.
(41) Garcia-Adeva, A. J. Band Structure of Photonic Crystals with the Symmetry of a Pyrochlore Lattice. *Phys. Rev. B: Condens. Matter Mater. Phys.* **2006**, *73*, No. 073107.
(42) Ducrot, É.; Gales, J.; Yi, G.-R.; Pine, D. J. Pyrochlore Lattice, Self-Assembly and Photonic Band Gap Optimizations. *Opt. Express* **2018**, *26*, 30052−30060.
(43) King, J. S.; Graugnard, E.; Summers, C. J. TiO_2 Inverse Opals Fabricated Using Low-Temperature Atomic Layer Deposition. *Adv. Mater.* **2005**, *17*, 1010−1013.
(44) Joannopoulos, J. D.; Johnson, S. G.; Winn, J. N.; Meade, R. D. *Photonic Crystals: Molding the Flow of Light*; Princeton University Press: Princeton, NJ, 2008.
(45) Shemi, O.; Solomon, M. J. Effect of Surface Chemistry and Metallic Layer Thickness on the Clustering of Metallodielectric Janus Spheres. *Langmuir* **2014**, *30*, 15408−15415.
(46) Ou, Z.; Luo, B.; Neophytou, A.; Chakrabarti, D.; Chen, Q. Synthesis and Self-Assembly of Janus and Triblock Patchy Particles. *Front. Nanosci.* **2019**, *13*, 61−85.
(47) Winfree, E.; Liu, F.; Wenzler, L. A.; Seeman, N. C. Design and Self-Assembly of Two-Dimensional DNA crystals. *Nature* **1998**, *394*, 539−544.
(48) Zheng, J.; Birktoft, J. J.; Chen, Y.; Wang, T.; Sha, R.; Constantinou, P. E.; Ginell, S. L.; Mao, C.; Seeman, N. C. From Molecular to Macroscopic *via* the Rational Design of a Self-Assembled 3D DNA Crystal. *Nature* **2009**, *461*, 74−77.
(49) Biffi, S.; Cerbino, R.; Bomboi, F.; Paraboschi, E. M.; Asselta, R.; Sciortino, F.; Bellini, T. Phase Behavior and Critical Activated Dynamics of Limited-Valence DNA Nanostars. *Proc. Natl. Acad. Sci. U. S. A.* **2013**, *110*, 15633−155637.
(50) Rovigatti, L.; Smallenburg, F.; Romano, F.; Sciortino, F. Gels of DNA Nanostars Never Crystallize. *ACS Nano* **2014**, *8*, 3567−3574.
(51) Bianchi, E.; Blaak, R.; Likos, C. N. Patchy Colloids: State of the Art and Perspectives. *Phys. Chem. Chem. Phys.* **2011**, *13*, 6397−6410.
(52) Gibson, K. D.; Scheraga, H. A. Crystal Packing without Symmetry Constraints. 1. Tests of a New Algorithm for Determining Crystal Structures by Energy Minimization. *J. Phys. Chem.* **1995**, *99*, 3752−3764.
(53) Togo, A.; Tanaka, I. *Spglib: A Software Library for Crystal Symmetry Search*, 2018; https://arxiv.org/abs/1808.01590 (accessed 2018-09-06).
(54) Whitelam, S.; Geissler, P. G. Avoiding Unphysical Kinetic Traps in Monte Carlo Simulations of Strongly Attractive Particles. *J. Chem. Phys.* **2007**, *127*, 154101.
(55) Whitelam, S.; Feng, E. H.; Hagan, M. F.; Geissler, P. G. The Role of Collective Motion in Examples of Coarsening and Self-Assembly. *Soft Matter* **2009**, *5*, 1251−1262.
(56) Růžička, Š.; Allen, M. P. Collective Translational and Rotational Monte Carlo Moves for Attractive Particles. *Phys. Rev. E* **2014**, *89*, No. 033307.
(57) Mériguet, G.; Jardat, M.; Turq, P. Structural Properties of Charge-Stabilized Ferrofluids under a Magnetic Field: A Brownian Dynamics Study. *J. Chem. Phys.* **2004**, *121*, 6078−6085.
(58) Steinhardt, P. J.; Nelson, D. R.; Ronchetti, M. Bond-Orientational Order in Liquids and Glasses. *Phys. Rev. B: Condens. Matter Mater. Phys.* **1983**, *28*, 784−805.
(59) Rein ten Wolde, P.; Ruiz-Montero, M. J.; Frenkel, D. Numerical Calculation of the Rate of Crystal Nucleation in a Lennard-Jones System at Moderate Undercooling. *J. Chem. Phys.* **1996**, *104*, 9932−9947.
(60) Errington, J. R.; Debenedetti, P. G. Relationship between Structural Order and the Anomalies of Liquid Water. *Nature* **2001**, *409*, 318−321.
(61) Chau, P.-L.; Hardwick, A. J. A New Order Parameter for Tetrahedral Configurations. *Mol. Phys.* **1998**, *93*, 511−518.
(62) Johnson, S. G.; Joannopoulos, J. D. Block-Iterative Frequency-Domain Methods for Maxwell's Equations in a Planewave Basis. *Opt. Express* **2001**, *8*, 173−190.

https://dx.doi.org/10.1021/acsnano.9b07849
ACS Nano 2020, 14, 5348−5359